Variable Buoyancy Data Transmitter, an Efficient Solution for Automated Spatiotemporal Marine Data Retrieval (2024)

Benjamin L.E Mallinson, School of Engineering, University of the West of England (UWE), Bristol (UK), Benjamin2.mallinson@live.uwe.ac.uk

***Abstract*— Advancements in machine learning based ecoinformatics offer significant opportunities for a wide range of marine conservation initiatives. However, the scalability is limited due to the high technological and labor costs of deploying and retrieving autonomous recording units (ARUs). Existing approaches fall into two dominant categories, bottom-mounted, which require expensive retrieval, and surface-floating, which, despite their ability to transmit data have problems with entanglement and tether noise. We propose a hybrid system where stored data from a bottom-mounted sensing station floats to the surface in a tethered module for transmission via satellite. The module is designed to adjust its buoyancy dynamically, increasing to surface and transmit data, then compressing to sink efficiently. As it compresses, it stores energy in the form of internal air pressure and elastic potential, this energy aids the expansion under pressure at depths where power generation is limited. We design and optimize an electromechanical test bed prototype to measure the system's power usage and determine the potential of such a device. In doing so, we simulate buoyancy adjustment and calculate force requirements to select a suitable configuration of components. We then test various elastic seal diaphragms and adjust tube length to optimize for performance down to 40m. The final prototype is used to measure power requirements and buoyancy forces. Results indicated that the device could be effectively powered from on board solar panels with minimal modification. This would generate enough power for the compression/decompression phases, LTE data upload, and motor driven retrieval by a seabed station The buoyancy force measured was in line with our simulations suggesting the device's capability to counteract tether drag in ocean currents.**

I. INTRODUCTION

The vast and largely unexplored marine ecosystems hold keys to understanding global biodiversity and its conservation. As these critical habitats face increasing threat, innovative technologies offer a beacon of hope, enabling us to uncover and safeguard the hidden complexities of marine life. Passive acoustic monitoring (PAM) devices are particularly prominent as they pay a crucial role in recording the intricate, species-specific, underwater soundscapes, providing invaluable data for mapping species richness, behavior, and habitat occupancy (Gibb, 2018). However, the scalability of these technologies is hampered by high operational costs and logistical challenges in data retrieval. By scaling this technology across various marine regions and integrating spatiotemporal data analysis, we can potentially detect ecological changes early, paving the way for proactive environmental interventions. As data driven biodiversity conservation efforts gain prominence, the applications of marine acoustic data are growing particularly fast (Mooney et al., 2022)

Research shows that traditional PAM technologies, as well as other forms of ARUs (e.g. photographic & eDNA), are limited to smaller scope passive conservation applications (Sugai, 2018; Ditria et al., 2022). This is predominantly due to challenges in physically collecting and managing the vast quantity of data created by high-frequency audio samples or video. The major bottleneck is the dense nature of water obstructing RF frequencies, thereby preventing traditional wireless data relay to surface-based stations.

Traditional solutions, depicted in Figure 1, utilize either direct data retrieval (Renata, 2013) or rely on data relay cables (Barnes et al., 2013; Mirimin et al., 2021). Methods requiring data collection include AUVs, animal tags, and seabed secured sensors. Data cable connected sensors can be tethered from a float, drone, boat, or a

sensor network. Although diverse, these methods share common challenges with either high operational costs or limitations in recording quality. For instance, surface tethered sensors can power themselves and transmit data but are prone to self-noise in recordings created by the tether, they also face challenges with entanglement of wildlife and boats. Submerged recorders offer improved audio clarity but necessitate physical data collection by resource intensive recovery teams. Innovations, such as an automatic weight release system (*Zitterbart et al., 2022*) and proton exchange membranes (Koc et al., 2023) have been introduced to minimize diving expenses. However, these methods are single use, so still rely on recovery vessels which represents a significant logistical challenge constraining the widespread application of these technologies.

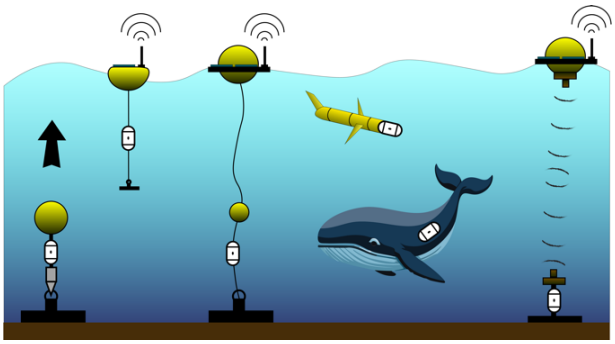

Fig. 1. Current and developing solutions.

Current Research acknowledges challenges with high-speed underwater wireless communication limits the scope of traditional PAM technologies. To address this issue, as well as the low power availability in these environments, emerging research has shifted focus to simultaneous wireless information and power transfer techniques. These methods include harnessing visible light in optical wireless power transfer (Filho et al., 2020), acoustic energy via piezoelectric backscatter (Afzal et al., 2022) and a novel opto-acoustic combination being explored using MIMO-OFDM (Pavalli, 2023). These methods show promising potential by utilizing different more suitable wave energies for underwater environments and using signal modulation via absorption and reflection to increase efficiency. However, this all these methods have inherent limitations with bandwidth and range. Also, they all require active signal generation which could potentially cause environmental pollution, directly affecting the marine life we are trying to conserve.

Our proposed solution, Figure 2, integrates a seabed mounted sensing station with a tethered buoyant transmission module that surfaces for data relay with a satellite. After transmission the module compresses itself for re-submersion and to enable energy efficient retrieval by the sensing station. This design innovatively leverages confined kinetic potential of compressed internal air and elastic potential stored in a diaphragm seal This stored energy assists expansion against opposing hydrostatic pressure at the seabed, critical due to the limitations of underwater power generation. By engineering a diaphragm with a specific stretch force, we optimize where energy generation is required, enabling the abundant solar energy at the surface to be utilized for expansion at the seabed.

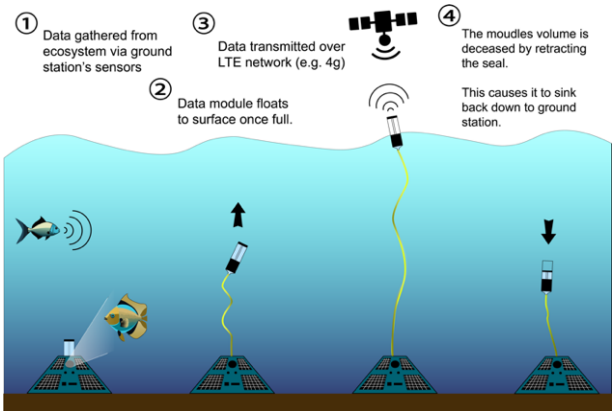

Fig. 2. Our proposed solution

As the tether unravels only during the surfacing process, we effectively eliminate self-noise and significantly mitigate risks of entanglement. This design promises a cost-effective, scalable method for the automated collection of pristine, high bandwidth data from marine environments.

II. Aim and Objectives

The aim of the project is to determine the potential of electromechanical volume adjustment as a low energy, low cost, and practical method for automatically retrieving large quintiles of data from underwater sensors.

To achieve the aim, we established the following objectives:

- Design and construct a developmental prototype of the variable buoyancy data module.
- Optimize the diaphragm and tube length on this design to enable minimal force for both expansion and contraction phases.

- Measure the power requirements for the maximum operational depth to determine the solar panel generation requirements.
- Measure the buoyancy force inversion to determine if its sufficient to counteract tether drag.

To assess the feasibility of our design we developed a test bed prototype of the variable buoyancy data module. This prototype is specifically engineered to measure the power requirements and operational efficiencies of our novel electromechanical design. We have chosen to exclude the data transmission hardware from this phase, considering its performance metrics are already well understood.

We selected a 40m operational depth for the prototype. This places our device in the transition zone between the Euphotic (0-30m) and mesophotic zones (30-150m). Species in these zones are particularly at risk from climate change due to coral bleaching. Organisms in deeper waters are generally considered more resilient and are largely dependent on bioproducts from healthy shallow water ecosystems, such as via the marine snow they often feed on (Alldredge & Silver, 1988; Smith, et al., 2009). By concentrating on the Euphotic zone, we aim to not only protect these at-risk populations but also indirectly support the conservation of deeper marine life through the preservation of their food sources.

In our design, energy gathered at the seabed that is not required for sensing travels through the tether cable to the data module to use for expansion. Similarly, excess energy harvested at the surface must be transmitted down to the sensing station. Given these dynamics, it is essential to understand the losses associated with energy transfer via a long cable as well as the charging system.

Ultimately, our goal is to predict whether the device can surface effectively with the additional challenges posed by water currents and drag induced from a neutrally buoyant cable. To inform this prediction we measure the device's ability to adjust its buoyancy. Evaluating this aspect is crucial for ensuring the device can reach the surface under typical operational conditions.

III. Design Methodology

In this section we recorded major steps in the initial design development process, the simulations used to predict and optimize buoyancy adjustment and the calculations we used to determine the major forces acting on the critical sealed piston head component.

Next, we describe our finalized CAD design as well as the electronic and mechanical component configuration.

Finally, we build the prototype and optimize it for efficient functional operation at depth.

A. Initial design

Figure 3, a finalized configuration illustration, is the outcome of an initial iterative prototyping and testing cycle (See Appendix).

We experimented with various methods of adjusting volume such as a piston and bellows. However, to ensure the system remains fully sealed and can operate at depth for long time spans we ended up selecting a top hat seal style design.

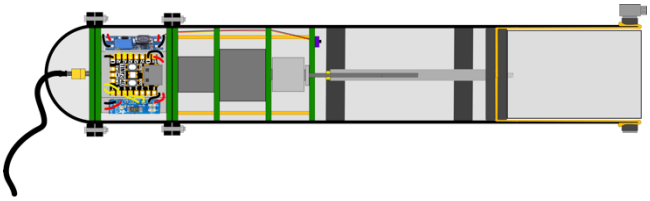

Fig. 3. Initial Illustration of chosen system configuration

The design compartmentalizes the outer tube into various sections. These are the End cap, Electronics, motor, gearbox, and force distribution. This section connects to the carriage via a lead screw, the carriage pulls back the diaphragm which is clamped around the end of the tube and restrained by an inner tube.

B. Simulations and Calculations

Buoyancy

Due to the necessity of efficiency, we chose to optimize the size and length of the device for its total mass. This would negate the need for extra weights/floats. This was done using a custom simulation. By calculating the volume of the tube and subtracting a smaller, internal, tube shape to represent the carriage compression a buoyant and weight force could be calculated to give us a net force. By sampling various reasonable tube lengths and parameters, we were able to choose a suitable tube for our expected mass range. We used python and matplotlib to create Figure 4. The final parameters we chose to meet all the requirements were:

External tube radius 0.025
Tube Wall thickness: 0.005
Material: Polycarbonate (1200 kg/m^3)
Internal Component mass (kg): 0.2- 0.4

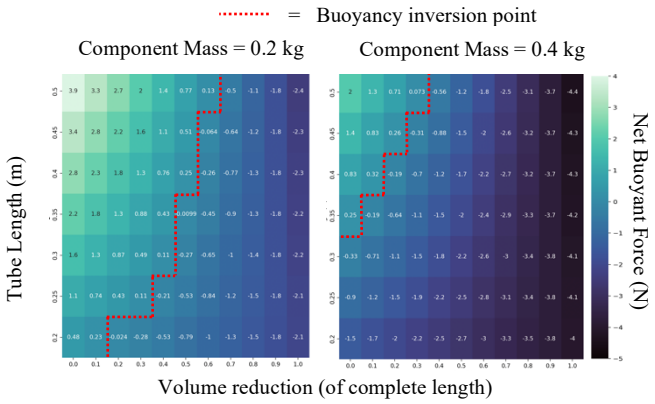

Fig. 4. Buoyancy simulation results

These initial simulations were done using a range of approximate internal component weights, a calculated weight for the tube at each size was added. This allowed for the buoyancy point to later be refined for the actual weight by adjusting the length of the tube in this range. We determined a radius of 0.025m, wall thickness of 0.005m, and length of 0.35m - 0.5m would provide optimal buoyancy inversion within 30% of volume reduction for component weights between 200g – 400g.

Hydrostatic Pressure Force

This force is pushing the seal inward and in increases with depth. To ensure the chosen motor and lead screw have enough torque to decompress at up to 40 m we first calculated the expected force on a seal of radius 19mm (-1mm for top hat seal gap spacing). Figure 5 describes the various pressures on the device when submerged and the force being calculated.

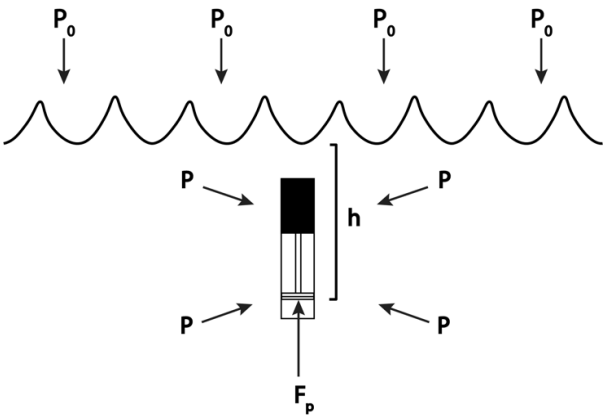

Fig. 5. Hydrostatic pressure force diagram

Hydrostatic pressure on submerged objects in an atmosphere can be calculated using pascals principle (1). The density of seawater at the surface, ρ, is approximately 1028.13 kg/m^3 (*Byrne, 2023).* Standard atmospheric pressure, P_O, at sea level is 101325 Pa (*Luebering, 2024).* Acceleration due to gravity was taken as 9.81 to calculate pressure acting on the module at the targeted depth of 40m in (2).

$$P = \rho g h + P_O \quad (1)$$

$$P = 1028.13 \times 9.81 \times 40 + 101325 \approx 504763\ Pa \quad (2)$$

To calculate the Force exerted by this pressure on the end of the plunger, we multiply pressure by area (3)

$$F_p = PA \quad (3)$$

Our requirements and simulation exploration determined an external radius of 25mm with a wall of 5mm would be an optimal tube size. With a 1mm gap for the top hat seal gap size our finalized plunger radius is 19mm. Using this, hydrostatic force at 40m was calculated (4).

$$F_p = 504763 \times (\pi \times 0.019^2) = 572.46\ \text{N} \quad (4)$$

Internal Air Pressure Force

Next, we calculated the opposing force created by the internal air pressure which increases as the module compresses itself.

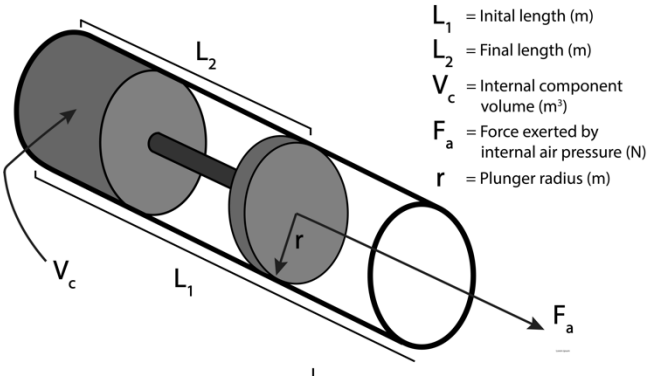

Fig. 6. Internal air pressure force diagram

Figure 6 depicts the variables we considered. Using our initial cad model for a 500 mm long design, we measured $L_1 = 0.406\ m$ & $L_2 = 0.256\ m$. We also calculated an estimated internal component volume $V_c = 1.23 \times 10^{-4}$.

$$V_1 = L_1 \pi r^2 - V_c$$

$$0.406(\pi \times 0.019^2) - 1.23 \times 10^{-4} = 3.38 \times 10^{-4}\text{m}^3 \quad (5)$$

$$V_2 = L_2 \pi r^2 - V_c$$

$$0.256(\pi \times 0.019^2) - 1.23 \times 10^{-4} = 1.68 \times 10^{-4}\text{m}^3 \quad (6)$$

Start and end volumes were calculated (5)(6). Using these values and Boyles law (7), rearranged in (8), final pressure was calculated (9). The Force exerted, F_a, was then calculated using (3), this results in 231.19N (10).

$$P_1V_1 = P_2V_2 \quad (7)$$

$$P_2 = \frac{P_1V_1}{V_2} \quad (8)$$

$$P_2 = \frac{101325\times3.38\times10^{-4}}{1.68\times10^{-4}} = 203856\ Pa \quad (9)$$

$$F_a = 203856 \times \pi \times 0.019^2 = 231.19\ \text{N} \quad (10)$$

Forces

To determine net force on the the piston we balanced all major forces, this is depicted in Figure 7.

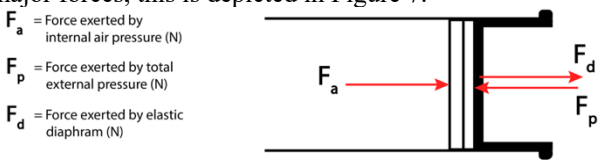

Fig. 7. Net force on diaphragm and plunger

At the surface $P = 0$, and, as the diaphragm is not under tension $F_d = 0$. So, total the external pressure force can be calculated (11)

$$F_p = P_o\pi r^2$$

$$F_p = (101325 \times \pi \times 0.019^2) = 114.91\ \text{N} \quad (11)$$

When compressing at the surface to begin the decent F_a will increase to 231.19N (10). Therefore, the maximum net force required to complete the compression at the surface is (12). This is the force our lead screw and motor must provide ignoring any additional diaphragm force for now.

$$F_{Surface} = F_p - F_a$$

$$F_{Surface} = 114.91 - 231.19 = \text{-}116.28\ \text{N}. \quad (12)$$

When decompressing at the seabed (40m) $F_p = 572.36\ N$ (4), F_a will still be equal to 231.19N. So, the lead screw force must be > 341.17 N (13).

$$F_{seabed} = 572.36\ 0 - 231.19 = 341.17\ N \quad (13)$$

To balance the requirements of the motor in compression and decompression at depth the diaphragm must be engineered to make up the difference (14).

$$F_d = \frac{F_{seabed} - F_{Surface}}{2} = \frac{341.17-116.28}{2} = 112.45\ N \quad (14)$$

Now, if we include the diaphragm force in the net force calculation (15), the required lead screw force for expansion and contraction are equalized (16)(17).

$$F_{net} = F_p - F_a - F_d \quad (15)$$

$$F_{surface} = 114.91 - 231.1 - 112.45 = 228.64\ N \quad (16)$$

$$F_{seabed} = 572.36 - 231.19 - 112.45 = 228.72\ N \quad (17)$$

Electromechanical requirements & Component Selection

Using our calculated force requirement of 228.72 and a lead screw with lead 2.54mm, we calculated the required torque for our motor-gearbox combination (18). An estimated transmission efficiency of 40% was assumed.

$$T = F \times \frac{L/1000}{2\pi E} = 228.72 \times \frac{2.54/1000}{2\pi\times0.4} = \ 0.231\ Nm \quad (18)$$

To provide this torque we selected a RE944 dc motor coupled with a 944D2311 planetary gearbox (Rs, 2024). This setup produces a torque of 0.245 Nm while remaining low cost with a suitable form factor for our design.

To transfer the motors torque to the carriage we selected a 6.35mm shaft Diameter trapezoidal lead screw and nut combination (Igus, 2015). A trapezoidal thread was chosen for its high load handling to ensure it can handle the force requirement, however if further testing proves this unnecessary a more efficient ball screw or high helix design could potentially be superior.

C. Design Documentation

In this section we describe the outcome of our iterative design exploration through the utilization of rapid prototyping and testing.

3D Modelling

Combining all the findings from our simulations and calculations to determine the optimal parameters and components lead us to a finalized design. Figure 8 shows an orthographic render of the CAD assembly.

Fig. 8. Render of fusion 360 model

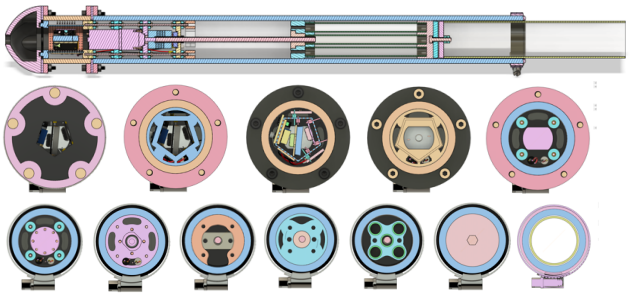

Fig. 9. Cross sections of the assembly

Using a modular design allows for easy assembly and maintenance. The cross sections in Figure 9 show internal features and correct assembly.

Electronics Schematic

We built our device from easily attainable off the shelf components for ease of replication. Figure 10 shows the electronic schematic of the whole setup

The system control and sensor interface are via a Tiny 2040 (pimoroni, 2021), which utilizes a RP2040 chip. This board was chosen for its small form factor for how it's representative of suitable hardware for a finalized version, with a low power arm architecture, high speeds, and impressive capabilities to enable edge computing and super-fast data transmission.

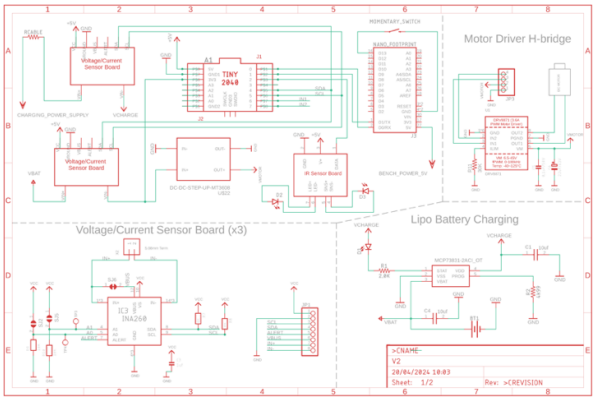

Fig. 10. Full circuit Schematic

Adafruit sensor boards (Siepert, 2019) were chosen as they come pre calibrated with a unique voltage reference and a nearly imperceptible 2 milliohm shunt resistor, ensuring highly accurate and precise readings. Using a shunt resistor ensures direct measurements with no effect from the motors Electromagnetic field.

The battery charging chip selected was the MCP73831 as it is readily available and suitable for efficient charging at low rates. This is integrated onto an LiPo Amigo board for the built in safety features (Pimoroni, 2022).

The motor is driven by a DRV8871 H-Bridge (Texas instruments, 2016), chosen as it utilizes N-channel MOSFETs instead of the transitional BJTs. This increases the power capability and improves efficiency. This is powered by a boost converter to enable a 12v supply from the 3.7v lithium polymer battery.

D. Build Documentation

Sections are joined with silicone gasket sealed flanges. 4 M2 brass threaded rods are used to clamp the motor, gearbox, and force distribution to 3d printed centering plates. Brass M2 nuts and washers are used for fastening along with rubber dampening washers. The mounting plates locate the mechanical subassembly in-between the silicone gasket sealed flange and the end stop plate.

Behind the mechanical module sits the electronics module, this is comprised of a pentagon of stripboard designed to fit the power, sensors, drivers, and control hardware into the smallest section of tube possible to maximize the devices buoyancy adjustment potential. Figure 11 shows a component breakdown and Figure 12 shows internal components and final assembly.

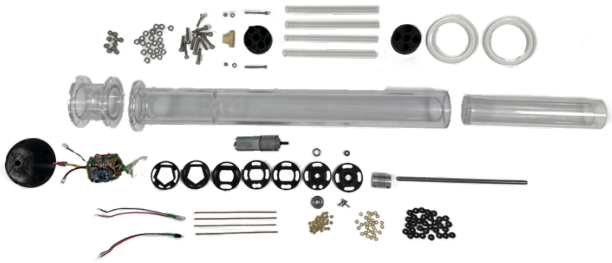

Fig. 11. Component breakdown photograph

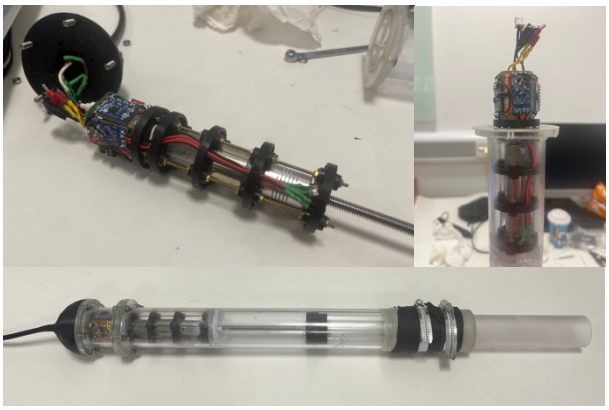

Fig. 12. Pictures of prototype

Buoyancy Optimization

To ensure the device inverted buoyancy within the right range of motion we adjusted our initial buoyancy simulation with updated data from the finalized design. As shown in Figure 13, a final weigh-in of all selected internal components was conducted. The accuracy of earlier tube weight calculations was also verified. We then ran the simulation for tube length increments of 0.01 m between 0.4 and 0.5 m which is the removable length we left in our design for refinement of the buoyancy point. Figure 14 shows the simulation results.

Final Internal component weight: 0.4kg

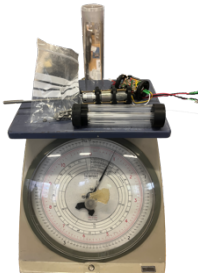

Fig. 13. Internal Component weigh in.

Internal weight 0.4kg

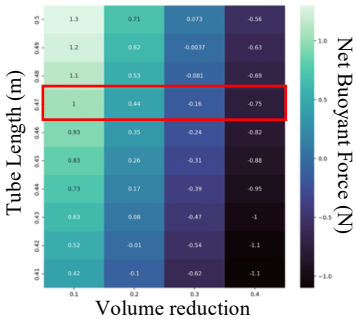

Fig. 14. Net buoyant force

With this information we selected a final tube length of 0.47m to provide an expected buoyant force, denoted as B, of 1N when fully expanded and -0.75N when sinking. We decided to aim for a slightly higher floating force than sinking to assist the device in dragging its cable to the surface, also, the sea-bed mounted station will be able to assist sinking via a cable spool. By subtracting the sinking from floating force, we determined this configuration should produce a buoyancy difference of 1.79N (19).

$$\Delta B = 1 - (-0.75) = 1.75\ N \qquad (19)$$

To balance the force in compression and decompression phases the diaphragm must require 112.45 N to fully stretch (14). To achieve this an elastomer 'top hat' seal was engineered. While many elastomers could potentially be suitable for a finalized production version, for the purposes of experimentation we chose to use latex as its readily available in the perfect shape in the form of condoms.

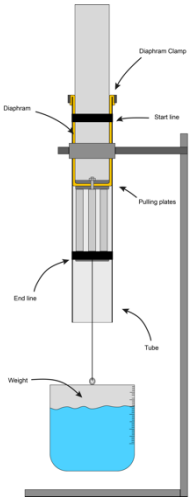

Fig. 15. Diaphragm test

We used the testing setup depicted in Figure 15 to determine the number of condoms required to create the requited elastic force of 112.45N when stretched to the end-mark, where the carriage will stop.

No. Diaphrams	Mass Requirement (kg)			Mean Mass (kg)	Mean Weight Force (N)
	Test 1	Test 2	Test 3		
1	1	0.9	0.9	0.93	9.16
2	2.3	2.3	2.4	2.33	22.89
3	4.5	4.4	4.5	4.47	43.82
4	5.5	5.7	5.7	5.63	55.26
5	7	7.2	7.1	7.10	69.65
6	8.5	8.7	8.7	8.63	84.69
7	10.7	10.5	10.2	10.47	102.68
8	12	11.5	11.6	11.70	114.78

Table. 1. *Diaphragm testing results*

Through our testing, photographed in figure 16, and documented in Table 1, we determined that eight, extra thick, condoms require 114.78N of force to stretch the required distance.

This is approximately the 112.45 N we calculated would enable balanced energy usage at the surface and seabed.

Fig. 16. Diaphragm testing setup

E. Testing Methodology

To test this idea and evaluate the potential of our design we defined a testing aim and some objectives:

Aim:

To determine the potential of the device to surface and submerge in under conditions. In doing so, ensure it is feasible to use the limited power available at the sea floor or during the surfacing time.

Objectives:

- Measure the change in buoyancy force created by a full inversion.
- Measure the power used by the device in compression and expansion phases.

Buoyancy Inversion Testing

To evaluate the potential for adjustment in buoyant force we measured the force in both sinking and floating modes to determine the total difference in buoyancy. The experimental setup included a water tank, lightweight string, a flat board, a weight, and a newton meter. Figure 17 is an illustration of the sinking setup.

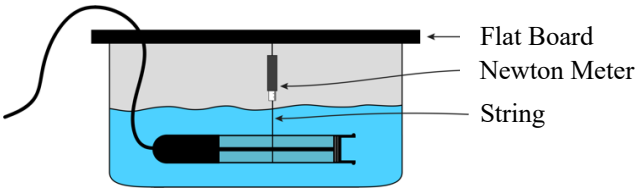

Fig. 17. Sink force testing setup.

Figure 18 depicts the floating measurement. In this test we submerged the force gauge, this required anchoring, we also measured the sinking force of the gauge itself to be subtracted from the measurement as the data module is required to lift this force in this configuration.

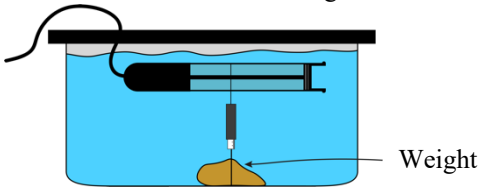

Fig. 18. Float force testing setup.

By securing the string and cable in place we controlled any effect they could have on results. We also conducted the test three times to help quantify any error caused by the measurement process or variations of the final carriage position.

Power Requirement Testing

We began by measuring the total energy requirement for compression and expansion at the surface using one of the on-board INA260 16-bit power sensors.
We recorded this data during inversion and expansion phases three separate times in high medium and low charge states to determine mean values and tolerances in the form of standard deviations.

The INA260 is capable of transmitting samples at up to 400khz (Texas Instruments, 2016) these are then averaged on the on the RP2040 running at up to 133MHz every 100ms (Raspberry Pi, 2019). These averages are subsequently transmitted over serial communication for storage and real time monitoring via a python program.

IV. Results

A. *Power requirements*

Figure 19 shows the first tests output from our real time power monitoring python program. These results are from the on-board sensor measuring the battery output so represent the total module power usage.

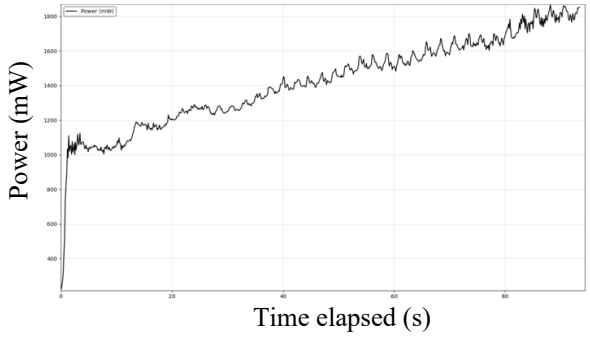

Fig. 19. Compression phase power monitoring

Figure 20 compares the decompression to the compression phase at the surface. We attain that in decompression the device is running at constant power, while this power is still high, we believe this is most likely mostly parasitic draw from initial testing of various h-bridge characteristics. In the test we found this MOSFET motor driver more is efficient under load than a BJT design, however it does require some additional parasitic power at low loads ($\approx 600mW$).

While the surface expansion test is not fully representative of real-world use at seabed, our balancing of forces via the engineering of the diaphragm means expanding at the seabed should use no more than the compression cycle does at the surface.

.

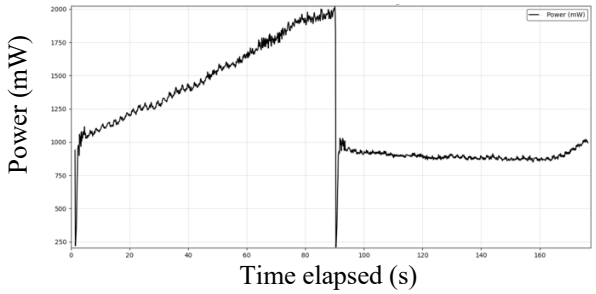

Fig. 20. *Compression and decompression cycle power*

The results were saved to Data_log_compressing.csv. By utilizing trapezoidal numerical integration on this data, we determined an estimation of total energy usage. We then averaged these values from all three tests and calculated the standard deviation, results are in Table 2.

Direction	Energy Required for inversion (J)			Mean Energy requirment (J)	Population Standered deviation (σ)
	Test 1	Test 2	Test 3		
Compression	112.402	112.61	108.23	111.0806667	2.017513541
Expansion	65.45	65.17	62.148	64.256	1.494957747

Table. 2. *Actuation energy requirement results*

B. *Buoyancy Inversion*

As described in our testing methodology, we measured the buoyancy force in fully compressed (sinking) and fully expanded (floating) configurations. The setup is photographed respectively in figures 21 and 22.

Fig. 21. *Compressed*

Fig. 22. *Expanded*

Mode	Net Boyant force (N)			Mean Boyant Force (N)	Population Standered deviation (σ)
	Test 1	Test 2	Test 3		
Floating	1.4	1.4	1.5	1.433333333	0.047140452
Sinking	-0.4	-0.2	-0.3	-0.3	0.081649658

Table. 3. *Net force results for buoyancy inversion test*

Results are show in Table 3. The buoyancy inversion point is slightly higher than simulated, this is likely due to differences in water salinity and the addition of flanges that was not accounted for in the simulation.

By subtracting the buoyancy force, for the sinking mode from the floating mode we get 1.733N difference (20).

$$\Delta B = 1.433 - (-0.3) = 1.733\ N \quad (20)$$

Encouragingly, this result is almost identical to the 1.75 N we predicted in our final buoyancy optimization simulation.

V. Discussion

The system works as expected and our power requirement results show potential. However, determining whether the outcome is sufficient for an operational solution requires some prediction for now and further testing in the future.

Energy required for surfacing.

Using our power monitor results we calculated the total on-board battery energy usage for a full surfacing and decent at 40m depth. This was done by doubling the balanced compression force on the surface as this should be equivalent to decompression at the seabed (21).

$$Energy_{Full\ cycle} = 111.08 * 2 = 222.16\ J \quad (21)$$

Sea floor power generation requirements

To calculate how many solar panels would be required we can assume a resurface charge time of one day will be more than frequent enough. As a watt is equal to 1 joule per second, to find the wattage required to create 222.16J in one day we can simply divide by the seconds in a day, however we use 6 hours instead of 24 to account for nighttime (22).

$$\frac{222.16}{6\times60^2} = 0.010285\ W \quad (22)$$

Even at the surface, solar panels don't provide 100% of their rating unless in ideal conditions, hence we divided by a harsh derating factor of 20% (23) to account for system inefficiencies, non-optimal panel angles, and panel degradation over long time periods.

$$\frac{0.010285}{0.2} = 0.051425\ W \quad (23)$$

This represents surface solar panel requirements for a full surfacing cycle power in one 6-hour day. However, to determine the seabed generation requirements we must also consider light attenuation in water. The flux intensity of light decays exponentially along direction z, from an initial intensity I_0 following the Beer-Lambert absorption law $I = I_0 \exp(-az)$. An average attenuation coefficient, a, for usable solar radiation (USR) for global coastal zones is taken as 0.65 m^{-1} (Lin et al., 2014). We then calculated an approximate factor of intensity reduction at for our maximum 40m operational depth (24).

$$\frac{I_{40}}{I_0} = e^{(-0.65*40)} = 5.109 \times 10^{-12} \quad (24)$$

We then divided our surface solar panel requirement (23) by this reduction factor to get the panel requirements for a one-day recharge at 40m (25).

$$\frac{0.051425}{5.109\times10^{-12}} = 1.007 \times 10^{10}\ W. \quad (25)$$

This massive result definitively rules out, sea-floor solar recharging of the system. The exponential attenuation of USR in marine environments in simply too great.

Surface charging power generation requirements

The novel appeal of our design is its ability to store energy within the system as it compresses, this opens the option of energy generation and storage at the surface where solar power is abundant. To calculate the panel requirements in this case we use a charge time of 30 minutes, representative of a predicted transmission time. We first calculated the power requirements (26) and then considered derating efficacy for solar panels (27).

$$\frac{222.16}{30*60} = 0.1234\ W \quad (26)$$

$$\frac{0.1234}{0.2} = 0.617\ W\ 9 \quad (27)$$

This demonstrates that for a full surface/decent charge in 30 minutes for actuation power alone would only require a 0.617 W panel. However, Data transmission hardware would require additional power, LTE transmitters use an approximate power of 1 W throughout upload (Caiazza et al., 2022), to account for this we calculated extra solar panel requirements at the surface (28).

$$\frac{1}{0.2} = 5\ W \quad (28)$$

Therefore, we could now calculate the minimum solar panel power rating required to power a 30-minute surface, transfer, and resubmission cycle (29)

$$0.617 + 5 = 5.617\ W \quad (29)$$

Fully integrated system solar panel requirements

Considering the final system, we must include power for a bottom mounted sensing station that is required to retrieve the module as it sinks as well as record and process the data itself. We assume the draw from the seabed stations motor is consistent with the results from our devices motor in expansion mode when it does not require a high torque, however this value can likely be optimized with a more suitable motor. This results in a 64.256 J each for the sinking and floating phases. The. total expected usage is calculated by doubling this value (30).

$$64.256 \times 2 = 128.512\,J \tag{30}$$

We must also consider losses in the cable. Power loss in a conductor can found with Joules Law (31).

$$P = I^2 \times R \tag{31}$$

For a copper cable with resistivity 1.68×10^{-8}, ρ, of radius 0.5mm, r, and length 40m, L, representative of commonly available neutrally buoyant cable suitable for the task, the cables resistance can be calculated (32).

$$R = \frac{\rho \times L}{A} = \frac{\rho \times L}{\pi r^2} = \frac{1.77 \times 10^{-8} \times 40}{\pi \times 0.0005^2} = 0.856\,\Omega \tag{32}$$

We can calculate an expected current (34) by first calculating the power needed to send required amount of energy in 30 minutes (33) and then dividing by the highest common solar panel voltage of 24V. Total energy loss can then be determined (35).

$$P = \frac{128.512}{30 \times 60} = 0.07139\,W \tag{33}$$

$$I = \frac{P}{V} = \frac{0.07139}{24} = 2.97 \times 10^{-3} A \tag{34}$$

$$P = (2.97 \times 10^{-3})^2 \times 0.856 = 7.57 \times 10^{-6}\,W \tag{35}$$

This result demonstrates the energy loss over the 40m cable is negligible (around a 0.1% drop) for a low current high voltage setup.

Therefore, to provide and transmit power for a retrieval motor the extra solar panel rating required can now be calculated (36).

$$\frac{0.07139}{0.2} = 0.357\,W \tag{36}$$

By summing the calculated solar panel ratings for both the data and seabed modules we can estimate the total solar panel rating requirement for a 30-minute surfacing data transfer and retrieval (37).

$$5.617 + 0.357 = 5.974\,W \tag{37}$$

Commonly available, low cost, 10 w monocrystalline, photovoltaic cells require approximately 600 cm^2 (Voltaic Systems, 2023), From our CAD model we determined the main tube alone has over 706.85 cm^2 of usable surface area, unmodified. This free space could be filled with solar panels to provide over a 10w rating power. Any excess energy generated could be sent down to the sea-bed station for use recording and processing data.

VI. Conclusion

In conclusion, we set out to determine the potential of a dc motor actuated, bouncy-adjusting data capsule for efficient marine data retrieval. To achieve this goal, we developed a developmental prototype, optimized for a depth of 40m. We then measured its buoyancy adjustment potential whilst using on board sensors to measure its energy usage.

Our tests confirmed the prototypes efficiency. However, generating solar power at the seabed proved impractical due to the exponential attenuation of light in water. Encouragingly, our findings indicate potential for abundant solar energy collection at the surface, which can be mechanically and kinetically stored in the device for later use. We demonstrated that this stored energy could not only support the devices operations but also supply excess power if the tube exterior were to be fully wrapped monocrystalline photovoltaic cells. Excess energy could be stored or sent down to the sensing station to be used for data recording and processing.

Buoyancy adjustment was in line with our initial simulations and enabled inversion from floating to sinking modes as simulated. This indicates that with further design optimizations (e.g. a compact custom PCB), the device could provide an even larger buoyancy adjustment with the same size. To definitively determine if the measured 1.73N adjustment potential is sufficient to overcome tether drag, future, deep-water, testing work is required, with the addition of a prototype seabed control station, spool, motor, and neutrally buoyant cable.

Other subsequent work should focus on the developing a fully functional prototype with transmission capabilities and developing and testing a design with materials which could withstand the harsh underwater environmental conditions for extended periods.

APPENDIX

Iterative design process sketches

Throughout our initial prototyping and testing phase we experimented with various configurations. Here we explain these iterations using developmental illustrations.

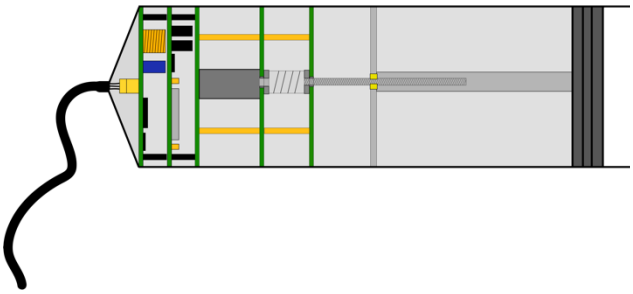

Fig. A1. First piston-based design.

Our first design, show in Figure A1, revolved around a syringe piston style mechanism. However, initial testing with premanufactured syringes informed us that the seal would not be adequate to remain air and watertight long term in harsh underwater conditions, as it relies on an oil-based lubrication to function.

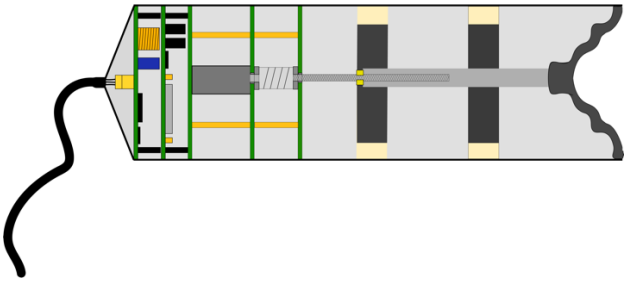

Fig. A2. Bellow based design.

As shown in Figure A2, to address the short comings of a moving piston we experimented with a pleated bellow style diaphragm that could expand/contract without any elastic deformation. This was successful but it was difficult to find any off the shelf components with the required amount of deformation.

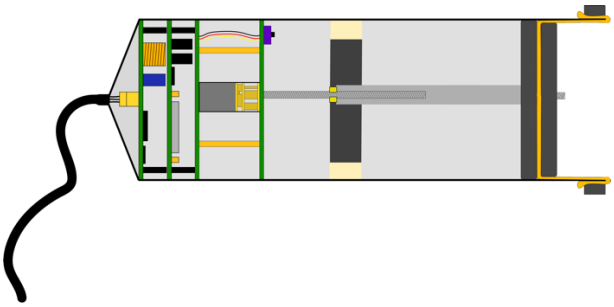

Fig. A3. First diaphragm seal based design.

To get the advantages of a sealed device but ensure the volume adjustment potential required we moved to diaphragm based design that elastically deforms with the piston, as illustrated in Figure A3.

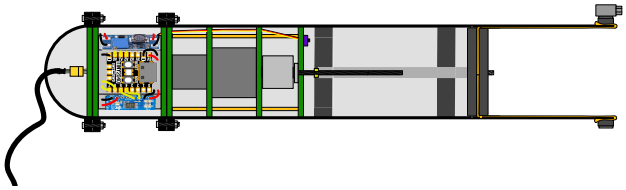

Fig. A4. Second diaphragm seal design.

Our initial diaphragm seal design showed promise, however, with this configuration it was difficult to get the volume adjustment required. For this reason, we extended the expected tube length range, this length modification is shown In figure A4.

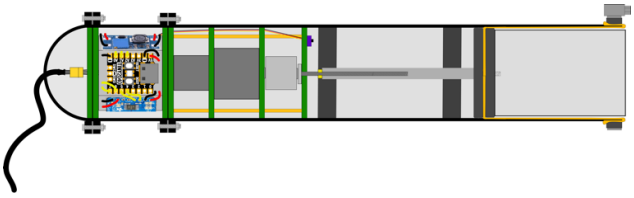

Fig. A5. Finalized 'top hat' seal design.

In our initial diaphragm testing we noticed a tendency to contract in the center when stretched, limiting the volume adjustment potential. For this reason, our final design utilized an internal tube to create a top hat seal that restrains the diaphragm when stretching.

REFERENCES

Afzal, S.S., Akbar, W., Rodriguez, O. et al. (2022) *Battery-free wireless imaging of underwater environments.* Nat Commun **13**, 5546. Available from*;* *https://doi.org/10.1038/s41467-022-33223-x (Accessed 10 March 2024]*

Alldredge, A., & Silver, M. (1988). *Characteristics, dynamics and significance of marine snow.* Progress in Oceanography, 20, pp. 41-82.

Barnes, C. R., Best, M. M. R., Johnson, F. R., Pautet, L., and Pirenne, B. (2013) *Challenges, Benefits, and Opportunities in Installing and Operating Cabled Ocean Observatories: Perspectives From NEPTUNE Canada, in* IEEE Journal of Oceanic Engineering, vol. 38, no. 1, pp. 144-157

Byrne, R.H., et al. (2023) Encyclopedia Britannica, *Density of seawater and pressure,* Available from: https://www.britannica.com/science/seawater/Density-of-seawater-and-pressure (Accessed 14th April 2024)

Caiazza, C., Giordano, S., Luconi, V., Alessio Vecchio, Edge computing vs centralized cloud: Impact of communication latency on the energy consumption of LTE terminal nodes, Computer Communications, Vol. 194, pp. 213-225

Ditria. E. M., Buelow, C. A., Gonzalez-Rivero, M., Connolly, R. M. (2022) *Artificial intelligence and automated monitoring for assisting conservation of marine ecosystems: A perspective,* Frontiers in Marine science, vol. 9

Filho, J. I. d. O., Trichili, A. B., Ooi, S., Alouini, M. -S. and Salama, K. N. (2020) *Toward Self-Powered Internet of Underwater Things Devices*, *IEEE Communications Magazine*, vol. 58, no. 1, pp. 68-73,

Gibbs, R., Browning, E., Glover-Kapfer, P., Jones, K. E. (2018) Emerging Opportunities and challenges for passive acoustics in ecological assessment and monitoring, Methods in Ecology and Evolution, vol. 10, 2, pp. 169-185

Igus (2015) *Trapezoidal leadscrew nut – Technical data* Available from: https://docs.rs-online.com/6d97/0900766b81418ca6.pdf (Accessed 27 April 2024)

Koc, D., Zuo, W., Ghorbel, F., and Chen, Z. (2023) "Energy Efficient Depth Control for Underwater Devices Using Soft and Hard Actuators," *2023 IEEE/ASME International Conference on Advanced Intelligent Mechatronics* pp. 916-921,

Lin, J., Lee, Z., Ondrusek, M., Kahru, M. (2016) *Attenuation coefficient of usable solar radiation of the global oceans*, Journal of Geophysical Research: Oceans, 121, 5, pp. 3228-3236

Luebering., J.E., et al. (2024) Encyclopedia Britannica, *Atmospheric pressure,* Available from: https://www.britannica.com/science/atmospheric-pressure (Accessed 14th April 2024)

Mirimin, L., Desmet, S., Romero, D., Fernandez, S., Miller, D., Mynott, S., Brincau, A., Stefanni, S., Berry, A., Gaughan, P., & Aguzzi, J. (2021). *Don't catch me if you can - Using cabled observatories as multidisciplinary platforms for marine fish community monitoring: An in situ case study combining Underwater Video and environmental DNA data.* The Science of the total environment, 773, 145351 .

Mooney, A., Lori, D. L, Lammers, M., Lin, T.-H, & Nedelec, S. L., Parsons, M., Radford, C., Urban, E., Stanley, J. (2020). *Listening forward: approaching marine biodiversity assessments using acoustic methods. Royal Society Open Science*. 7. 201287

Pallavi, Ch, & Sreenivasulu, G.. (2023). *Performance of a MIMO-OFDM-Based Opto-Acoustic Modem for High Data Rate Underwater Wireless Communication (UWC) System*. Advances in signal processing, embedded systems, and IoT, pp. 51-56

Pimoroni (2022) *LiPo Amigo (LiPo/LiIon Battery Charger) – LiPo Amigo, Available from: https://shop.pimoroni.com/products/lipo-amigo?variant=39779302506579 [Accessed 19 April 2024]*

Raspberry Pi, (2019) RP2040 Datasheet, a microcontroller by Raspberry Pi, Available from: https://datasheets.raspberrypi.com/rp2040/rp2040-datasheet.pdf [Accessed 18 April 2024]

Renata, S. -L., Deborah, F., Thomas, N., Julie, O. (2013) A review and inventory of fixed autonomous recorders

for passive acoustic monitoring of marine mammals. Aquatic Mammals. Vol 39, pp.23-25

Rs Pro (2024*) Brushed Dc geared motor, 1.5W, 12V dc, 25Ncm, 29rpm, 4mm shaft Diameter*. Available from https://uk.rs-online.com/web/p/dc-motors/0420637 (Accessed 27 April 2024)

Siepert, B. (2019) *Adafruit INA260 High or Low Side Current and Power Sensor PCB*, Available from: https://github.com/adafruit/Adafruit-INA260-PCB [Accessed 19 April 2024]

Smith, K. L., Jr, Ruhl, H. A., Bett, B. J., Billett, D. S. M., Lampitt R. S. and Kaufmann R. S. (2009) *Climate, carbon cycling, and deep-ocean ecosystems*. Available from: https://www.pnas.org/doi/full/10.1073/pnas.0908322106 (Accessed 26th April 2024)

Sugai, L. S. M., Silva, T. S. F., Ribeiro, J. W., Llusia, D. (2019) *Terrestrial Passive Acoustic Monitoring: Review and Perspectives*, *BioScience*, Volume 69, Issue 1, January 2019, pp. 15–25

Texas Instruments (2016) *Ina-260 Datasheet, Precision Digital Current and Power Monitor With Low-Drift, Precision Integrated Shunt*, Available from: https://www.ti.com/lit/ds/symlink/ina260.pdf%C2%A7 [Accessed 18 April 2024]

Texas instruments (2016) *DRV8871 3.6-A Brushed DC Motor Diver With Internal Current sense* (PWM Control), Available from: https://www.ti.com/lit/ds/symlink/drv8871.pdf?ts=1714226046813&ref_url=https%253A%252F%252Fwww.ti.com%252Fproduct%252FDRV8871 (Accessed 27 April 2024)

Zitterbart, D.P., Alessandro, B., Ochs, M., Bonnel, J. (2022) TOSSIT, *A low-cost, hand deployable, rope-less and acoustically silent mooring for underwater passive acoustic monitoring,* Available from: https://www.sciencedirect.com/science/article/pii/S246067222000499 [Accessed 10 March 2024]